Research Article Vol. 29, No. 3 / 1 February 2021 / Optics Express 3342

Optics EXPRESS

# Coherent Fourier scatterometry using orbital angular momentum beams for defect detection

Bin Wang,[1,2] Michael Tanksalvala,[1,2] Zhe Zhang,[1,2,3] Yuka Esashi,[1] Nicholas W. Jenkins,[1,2] Margaret M. Murnane,[1,2] Henry C. Kapteyn,[1,2,4] and Chen-Ting Liao[1,2,*]

[1] *JILA, University of Colorado and NIST, 440 UCB, Boulder, Colorado 80309, USA*
[2] *STROBE Science and Technology Center, JILA and Department of Physics, University of Colorado, Boulder, Colorado 80309, USA*
[3] *MOE Key Laboratory of Advanced Microstructural Materials, Institute of Precision Optical Engineering, School of Physics Science and Engineering, Tongji University, Shanghai 200092, China*
[4] *KMLabs Inc., 4775 Walnut St. Building 102, Boulder, Colorado 80301, USA*
[*] *ChenTing.Liao@colorado.edu*

**Abstract:** Defect inspection on lithographic substrates, masks, reticles, and wafers is an important quality assurance process in semiconductor manufacturing. Coherent Fourier scatterometry (CFS) using laser beams with a Gaussian spatial profile is the standard workhorse routinely used as an in-line inspection tool to achieve high throughput. As the semiconductor industry advances toward shrinking critical dimensions in high volume manufacturing using extreme ultraviolet lithography, new techniques that enable high-sensitivity, high-throughput, and in-line inspection are critically needed. Here we introduce a set of novel defect inspection techniques based on bright-field CFS using coherent beams that carry orbital angular momentum (OAM). One of these techniques, the differential OAM CFS, is particularly unique because it does not rely on referencing to a pre-established database in the case of regularly patterned structures with reflection symmetry. The differential OAM CFS exploits OAM beams with opposite wavefront or phase helicity to provide contrast in the presence of detects. We numerically investigated the performance of these techniques on both amplitude and phase defects and demonstrated their superior advantages—up to an order of magnitude higher in signal-to-noise ratio—over the conventional Gaussian beam CFS. These new techniques will enable increased sensitivity and robustness for in-line nanoscale defect inspection and the concept could also benefit x-ray scattering and scatterometry in general.



## 1. Introduction: scatterometry for defect inspection

Optical and x-ray scatterometry are indispensable tools for metrology critical to modern nanodevice manufacturing. In particular, the detection of nanoscale defects on photolithographic substrates, reticles, masks, and wafers is a critical quality control used in all semiconductor foundries [1,2]. Wafers and reticles are routinely inspected using visible or ultraviolet beams, both in reflection and transmission, to spot feature size corresponding to the 22 nm technology node and smaller in the in-line process. Additional tools such as scanning probe or electron beam imaging are then used off-line to inspect smaller regions of interest, to enhance resolution, and more precisely locate the defect. Moreover, to support extreme ultraviolet (EUV) lithography at $\lambda = 13.5$ nm, sensitivity to smaller defects is needed. Locating and classifying defects with in-line measurements is desirable to reduce the need for removal of the wafer from the fabrication line. Using an ArF excimer laser at 193 nm deep UV wavelength, commercial non-imaging scatterometry instruments are sensitive to defects as small as 10 nm, corresponding to a resolution of $\sim\lambda/20$ [3]. Incoherent laser-produced plasma sources in the EUV and soft x-ray regions can also be used as scatterometry reference standards for model-based metrology [4–6].

#414584 https://doi.org/10.1364/OE.414584
Journal © 2021 Received 12 Nov 2020; revised 24 Dec 2020; accepted 28 Dec 2020; published 20 Jan 2021

Optics EXPRESS

Tabletop-scale high harmonic generation (HHG) can be used to create light in the UV, EUV, and soft x-ray regions, λ ~1-100 nm [7–9] using an extreme nonlinear optical process that up-converts photons from a femtosecond laser. In contrast to laser-produced plasma sources, HHG beams are fully spatially and temporally coherent, and as such, are an ideal short-wavelength light source for spectroscopy, scatterometry, and coherent imaging. Sub-wavelength resolution EUV imaging has already been demonstrated using HHG in a full field computational coherent imaging modality, and furthermore this source has been used to capture the fastest charge and spin dynamics in materials and other systems, on attosecond to femtosecond timescales [10–15].

Coherent Fourier scatterometry (CFS) is an in-line metrology technique based on far-field diffraction of a tightly-focused coherent laser beam, that is scanned across a sample. The presence of a defect will result in changes in the far-field scatter pattern that can be detected. CFS was originally used to characterize the shape and position of grating structures and has also been shown to have strong capabilities for detecting nanoparticles on silicon, glass, and plastic substrates [16,17]. Conventionally, CFS inspection of semiconductor samples uses a Gaussian laser beam as the illumination. It is a model-based technique that employs a library search strategy, where *a priori* knowledge about the sample, as well as of the likely types of defects, is required. CFS can be implemented in a dark-field or bright-field modality. Dark-field CFS techniques block the specular reflection and capture only the remaining high-angle scattered light. These dark-field techniques allow for sensitive detection of deep sub-wavelength scale defects because large-angle scattering is more affected by the defect than small-angle scattering. CFS using visible lasers has proven to have sensitivity adequate for the 12 nm technology node and above [18]. However, the incident illumination power must be very high to achieve the threshold signal-to-noise ratio (SNR) for confident detection, which in turn may unavoidably damage the sample due to induced thermal and chemical effects. In contrast, bright-field CFS techniques, which collect both the specular reflection and high-angle scattering, require much lower incident power and do not suffer from the radiation damage problem. However, the small inherent scattering and low-SNR limits the sensitivity, such that sub-100 nm defects are difficult to detect using visible light alone.

Recently, the generation of laser light with orbital angular momentum (OAM) [19] has attracted considerable interest because of its potential applications for enhanced optical sensing, imaging, and high-bandwidth communication [20–22]. Several works have also shown that laser beams carrying OAM can be upconverted into the EUV using the HHG process, imprinting either static or time-varying OAM [23–25]. OAM in light corresponds to a macroscopic property of the scalar field spatial distribution that can impart angular momentum, distinct from field polarization. OAM beams have a helix-shaped wavefront with an optical vortex at the center and are characterized by an integer quantum number $q$, called the OAM charge or topological charge of light. The sign of $q$ determines the handedness of the helical wavefront. The OAM charge can be measured using interferometry, diffraction through a triangular aperture, or coherent diffractive imaging, among other techniques [26–28]. The diffraction of an OAM beam from a sample will show distinct signatures different from what would be observed using a simple Gaussian beam. Moreover, the diffraction patterns from a sample with defects illuminated by two OAM beams with opposite phase front helicity, namely, opposite OAM value, show different signatures. This allows us to demonstrate differential CFS as a new metrology technique for defect inspection, where diffraction patterns using two OAM beams of opposite helicity are compared to detect defects, as opposed to comparing to a reference. In scatterometry, a simple structured illumination with a binary phase structure was recently used to enhance the detection of nanoscale grating asymmetry and overlay error [29,30]. Our OAM beam CSF is inspired by structured illumination microscopy, which enhances imaging performance by utilizing illuminations with specifically designed amplitude or phase structures. A big advantage of using OAM beams is that OAM modes are exact propagating solutions—Laguerre-Gaussian modes—to the wave equation in

Optics EXPRESS

a circularly symmetric beam. This property contrasts with arbitrarily structured illumination, which may not necessarily be an eigen solution to the paraxial wave equation and could lead to significant wavefront property change right after propagation and diffraction.

To solve the problem of high-sensitivity, high-throughput, and in-line nanoscale defect detection with minimal radiation damage, we combine bright-field CFS techniques with OAM beams and numerically investigate their performance. The paper is organized as follows: Section 2 introduces the new CFS techniques using OAM beams. In Section 3, the sensitivity enhancement of OAM beam-based CFS is discussed, and two data processing techniques based on the detection of asymmetry in far-field diffraction patterns are proposed. Numerical simulations are conducted to compare the performance of CFS techniques using Gaussian and OAM beams. Finally, we conclude the paper in Section 4.

## 2. Coherent Fourier scatterometry techniques

We first review conventional bright-field CFS illuminated with a Gaussian spatial profile beam, which is one of the widely applied methods for defect inspection where radiation, thermal, or and chemical effects induced damages from high power beams need to be avoided. We then propose three new bright-field CFS techniques using OAM beams as the illumination.

### 2.1. Model-based CFS using a Gaussian beam

In conventional model-based CFS using a Gaussian beam (referred to as model-based Gaussian CFS), a spatially coherent Gaussian beam is scanned across a sample under inspection. The far-field diffraction patterns, $I_{q=0}(f_x,f_y)$, are measured and compared with reference patterns from a pre-established database, $I_r(f_x,\ f_y)$, to determine whether defects are present in the area of the illumination. Note that a $\text{TEM}_{00}$ Gaussian beam can be regarded as a special OAM beam with $q = 0$. Furthermore, it is possible to use the difference between $I_{q=0}(f_x,\ f_y)$ and $I_r(f_x,\ f_y)$ to locate the defect with respect to the beam center without additional measurements. In Fig. 1, the sample under inspection, represented as either the complex reflectivity or transmissivity, in the sample plane, $O(x, y)$, can be modeled as the sum of a defect-free sample, $S(x, y)$, and a small additive defect, $D(x, y)$, *i.e.*, $O(x, y) = S(x, y) + D(x, y)$. The defect-free sample is usually a uniform planar substrate and the additive defect is one of the most common cases, representing an unwanted particle or contamination on the planar substrate. Given a coherent Gaussian beam as the illumination, $P_{q=0}(x, y)$, the far-field diffraction patterns measured on the detector plane can be written as:

$$\begin{aligned} I_{q=0}(f_x,f_y) &= |\Im\{[S(x,y) + D(x,y)]P_{q=0}(x,y)\}|^2 \\ &= |\Im\{S(x,y)P_{q=0}(x,y)\}|^2 + |\Im\{D(x,y)P_{q=0}(x,y)\}|^2 \\ &\quad + \Im\{S(x,y)P_{q=0}(x,y)\}\Im\{D(x,y)P_{q=0}(x,y)\}^* \\ &\quad + \Im\{S(x,y)P_{q=0}(x,y)\}^*\Im\{D(x,y)P_{q=0}(x,y)\}, \end{aligned} \tag{1}$$

where * represents the complex conjugate and $\Im$ represents the Fourier transform operation. Here we model the light-matter interaction as a single scattering event and treat the light propagation from the sample plane to the far-field detector plane using Fraunhofer diffraction. The corresponding reference diffraction pattern from the defect-free sample on the detector plane is $I_r(f_x,f_y) = |\Im\{S(x,y)P_{q=0}(x,y)\}|^2$, and the difference between the measured and reference pattern $\Psi(f_x,f_y)$ is:

$$\begin{aligned} \Psi(f_x,f_y) &= I_{q=0}(f_x,f_y) - I_r(f_x,f_y) \\ &= |\Im\{D(x,y)P_{q=0}(x,y)\}|^2 \\ &\quad + \Im\{S(x,y)P_{q=0}(x,y)\}\Im\{D(x,y)P_{q=0}(x,y)\}^* \\ &\quad + \Im\{S(x,y)P_{q=0}(x,y)\}^*\Im\{D(x,y)P_{q=0}(x,y)\}. \end{aligned} \tag{2}$$

Optics EXPRESS

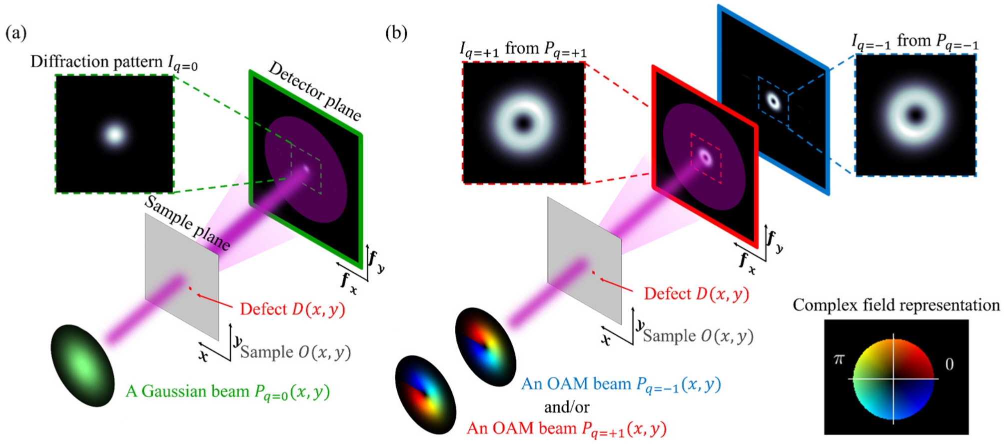


**Fig. 1. Schematic of coherent Fourier scatterometry techniques using different illumination beams.** (a) Model-based Gaussian CFS. A Gaussian beam illuminates a defect-free sample $O(x,y)$, which is chosen to be a uniform planar substrate for discussion, with a point defect $D(x,y)$, marked in red, and the far-field diffraction patterns, $I_{q=0}$, are recorded on the detector plane. The complex wavefront of the Gaussian beam $P_{q=0}(x,y)$ is plotted with amplitude and phase being represented as brightness and hue, respectively, as shown in the color wheel of the inset. The green dashed box shows the center of the diffraction pattern. (b) Model-based OAM CFS, model-based differential OAM CFS, and model-free OAM CFS. All three techniques share the same experimental setup but differ in data collection and processing. When illuminating with a single OAM beam $P_q(x,y)$ with integer OAM charge $q=+1$ or $q=-1$, the resulting diffraction pattern, $I_q$, is shown in the red or blue solid boxes, respectively. Note that the diffraction patterns from OAM beams exhibit an obvious asymmetry, which can be leveraged to perform defect inspection. A Gaussian beam can be regarded as a special OAM beam with $q=0$. All beams share the same complex field representation.

In the case where defects are minuscule in comparison to the beam size, the first term on the right-hand side of Eq. (2) is negligible, and the defect can be approximated by a $\delta$ function, *i.e.*, $D(x,y)=c\delta(x-x_0,y-y_0)$, where $c$ is a complex scaling factor and $(x_0,y_0)$ is the coordinate of the defect. The inverse Fourier transform of $\Psi(f_x,f_y)$ yields the defect location map $\psi(x,y)$, which reads:

$$\begin{aligned}\psi(x,y) &= \mathfrak{I}^{-1}\{\Psi(f_x,f_y)\}\\ &= c^*S(x+x_0,y+y_0)P_{q=0}(x+x_0,y+y_0)P_{q=0}(x_0,y_0)^*\\ &\quad+\ cS(-x+x_0,-y+y_0)^*P_{q=0}(-x+x_0,-y+y_0)^*P_{q=0}(x_0,y_0).\end{aligned} \tag{3}$$

Equation (3) consists of two terms. The first term is proportional to the field from the defect-free sample, $S(x,y)\cdot P_{q=0}(x,y)$, shifted by $(-x_0,-y_0)$. The second is proportional to the complex conjugate of $S(x,y)\cdot P_{q=0}(x,y)$, rotated by 180° and shifted by $(x_0,y_0)$. Since these two terms are centered at the defect location and its mirror location about the origin, their centroids are possible locations of the defect. Consequently, there is an inherent two-fold ambiguity in the determined defect location.

Figure 2 shows the CFS data recording and processing flow for both Gaussian and OAM beam based CFS. For model-based Gaussian CFS (the first column of Fig. 2), a Gaussian beam illuminating a uniform sample with a point defect (the white dot pointed by the red arrow) seen in the sample plane is shown in Fig. 2(a). All subfigures, including those on the sample plane and the defect location maps, are plotted with amplitude and phase being represented as brightness and hue, respectively. The 4-step data recording and process flow include:

(1) Illuminate the sample with a Gaussian beam,

(2) Record a far-field diffraction pattern,

(3) Subtract the recorded pattern from the reference pattern,

(4) Inverse Fourier transform the difference.

We then obtain the defect location map $\psi(x, y)$ as shown in Fig. 2(b), which contains the two ambiguous terms introduced in Eq. (3), the two possible defect locations, as indicated by the orange arrows.

### 2.2. Model-based CFS using an OAM beam

In the model-based OAM CFS, we use an OAM beam with an OAM value of $q$ to replace the Gaussian beam as the illumination, as shown in Fig. 1(b). Because of its intrinsic spiral phase structure, the OAM beam will break the symmetry in diffraction patterns $I_q(f_x, f_y)$, which can be leveraged to perform sensitive defect inspection. Note that Eqs. (1-3) are general mathematical expressions, regardless of the illumination type. Figure 2(c) shows an OAM beam with $q = +1$ incident onto a uniform sample with a point defect (the white dot indicated by the red arrow). After performing a similar 4-step data recording and process as described in the previous subsection 2.1, we get the defect location map $\psi(x, y)$ shown in Fig. 2(d). The map appears to have the same features as in Fig. 2(b), but the two ambiguous terms have opposite handedness in phase. Therefore, we break the inherent two-fold ambiguity, allowing us to determine the correct defect localization. As indicated in Eq. (3) and by the orange arrow in Fig. 2(d), the center of the component that has the opposite handedness to that of the OAM beam indicates the correct defect location.

To better understand the benefits of using OAM beams, we develop an intuition for why OAM beams cause symmetry breaking in diffraction patterns by comparing the characteristics of diffraction patterns from Gaussian and OAM CFS. We consider a uniform substrate, $S(x, y)$, with a small additive amplitude-only defect, which can be expressed as $D(x, y) = r\delta(x - x_0, y - y_0)$, where $r$ is the defect amplitude and $(x_0, y_0)$ is the location of the defect on the sample plane. The defect amplitude here means the magnitude of the normalized complex reflectivity or transmissivity of the defect in reflection or transmission geometries, respectively, and thus $r$ varies between 0 and 1. The sample is illuminated by a coherent Gaussian or OAM beam, $P_q(x, y)$, while the point defect is assumed to be located to the right of the beam for the discussion. The far-field diffraction pattern is written in Eq. (1). The first and second terms on the right-hand side of Eq. (1) are the intensity distribution of the complex electromagnetic fields resulting from the defect-free substrate and the defect, *i.e.*, $\Im\{S(x, y)P_q(x, y)\}$ and $\Im\{D(x, y)P_q(x, y)\}$, which we will refer to as the substrate field and defect field, respectively. The third and fourth terms denote the interference intensity pattern between the substrate and defect fields, which is real and we will refer to as the "interference intensity pattern". Figure 3 shows these fields individually for both Gaussian and OAM CFS to better understand the difference in their diffraction patterns. The simulated Gaussian and OAM beams are set such that their peak intensity and integrated power are both the same.

For a Gaussian beam at focus, *i.e.*, with a flat wavefront, the complex substrate and defect fields are shown in Fig. 3(a) and 3(b). The horizontal linear phase in Fig. 3(b) is caused by the shift of the defect to the right in real space relative to the center of the illumination beam. Figure 3(c) shows the interference intensity pattern, which is real and symmetric. The final far-field diffraction pattern is the summation of the intensity of substrate and defect fields and the interference intensity pattern, which is shown in Fig. 3(d). Similarly, the complex substrate and defect fields, the interference intensity pattern, and the far-field diffraction pattern from the OAM beam at focus with $q = +1$ are shown in Figs. 3(e)–3(h). As clearly shown in the inset of

Optics EXPRESS

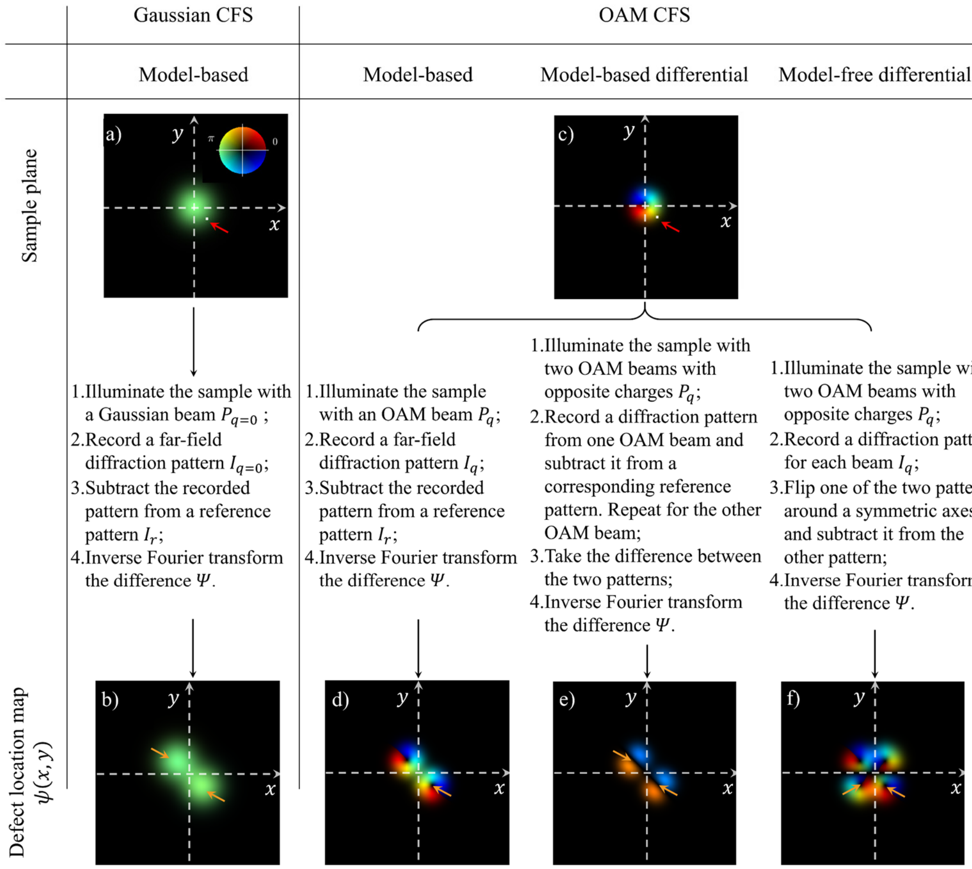


**Fig. 2. CFS data recording and processing flow, including conventional Gaussian CFS (first column) and OAM beam based CSF (second, third, and forth columns).** On the sample plane, an illumination incident onto a sample, which is chosen to be a uniform planar substrate for discussion, with a point defect (the white dot pointed by the red arrow) are shown in (a) and (c) for a Gaussian and an OAM beam with $q = 1$, respectively. After the four-step CFS data processing, we get a defect location map $\psi(x, y)$ as shown the last row. In (b), the map contains two terms that are centered at two potential defect locations, indicated by the two orange arrows, and is symmetric about the origin, leading to a two-fold ambiguity. (d) In model-based OAM CFS, the defect location map appears to be similar to that in the model-based CFS, however, these two terms have opposite handedness in phase. We thus can use this unique feature to break the ambiguity and determine the correct defect location, as indicated by the orange arrow. (e) In model-based Differential OAM CFS, the defect map again have two ambiguous terms. (f) In model-free Differential OAM CFS, the map shows four ambiguous terms. Using several symmetric axes and point, as well as the phase handedness, we can then determine the potential defect locations with just two ambiguous terms, as indicated by the two orange arrows. In (b, e, f), we can further use other constraints such as the scanning pattern to break the two-fold ambiguity and determine the final defect location. All figures are plotted with amplitude and phase being represented as brightness and hue, respectively.

Optics EXPRESS

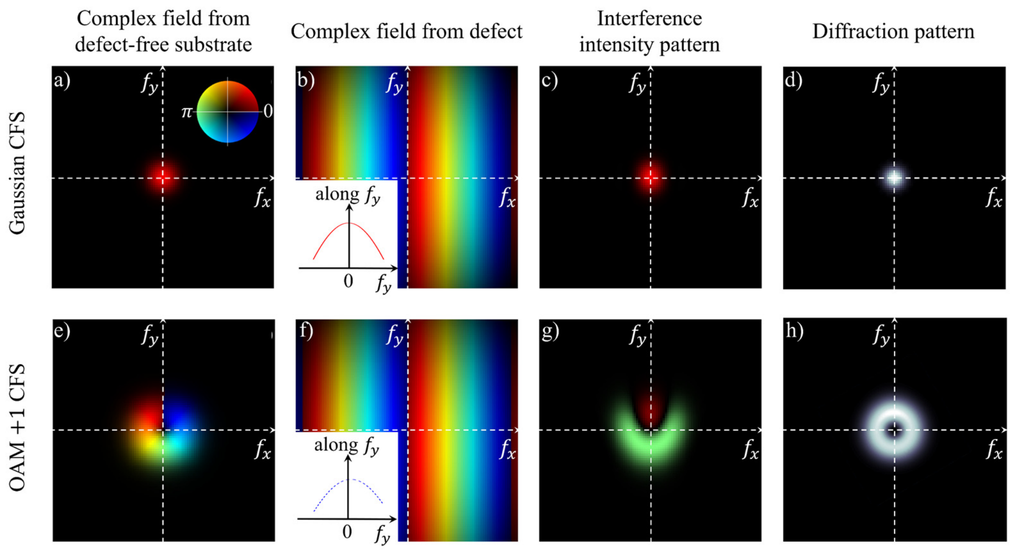


**Fig. 3. The characteristics of far-field diffraction patterns from Gaussian and OAM beams illuminating on blank substrate with amplitude-only defects.** (a) and (b) show the complex fields from the defect-free substrate and from the defect, *i.e.*, $\Im\{S(x,y)P_q(x,y)\}$ and $\Im\{D(x,y)P_q(x,y)\}$ in Eq. (1), in the far-field from Gaussian CFS. The defect is assumed to be located to the right of the beam for the discussion. The inset of (b) shows the amplitude of the defect field for Gaussian CFS along $f_y$ axis and it is symmetric. (c) shows the interference intensity pattern, i.e., $\Im\{S(x,y)P_{q=0}(x,y)\}\Im\{D(x,y)P_{q=0}(x,y)\}^* + \Im\{S(x,y)P_{q=0}(x,y)\}^*\Im\{D(x,y)P_{q=0}(x,y)\}$, and (d) shows the far-field diffraction pattern, which is the summation of intensity of the substrate and defect fields, and the interference intensity pattern. Similar plots for OAM $\pm 1$ CFS are shown in (e-h). The inset of (f) shows the amplitude of the complex field from defect for OAM CFS along $f_y$ axis, and it is not symmetric because of the spiral phase of OAM beams. The interference intensity pattern of OAM CFS in (g) shows significant asymmetry due to the spiral phase of the OAM beam. This asymmetry further propagates into the far-field diffraction pattern, as shown in (h). The color wheel for complex field representation is shown in the top right corner of (a), where amplitude and phase are represented by brightness and hue, respectively. See Visualization 1 and Visualization 2 for using Gaussian and OAM beams to scan the defect phase from 0 to $\pi$, respectively.

Fig. 3(f), the defect field is not centered in $f_y$ direction. This is because the small defect sees the local spiral phase from the OAM beam approximately as a linear phase — consequently, in frequency space, the field is shifted away from the center according to the Fourier shift theorem. Moreover, the interference intensity pattern, shown in Fig. 3(g), shows significant asymmetry in the vertical direction. It is the locally linear, while the globally spiral phase of the OAM beams that result in the asymmetry in the complex defect field and the interference intensity pattern, thus causing significant asymmetry in diffraction patterns as shown in Fig. 3(h). This asymmetry can also be seen in the diffraction patterns in the red and blue dashed boxes in Fig. 1(b).

In fact, the amplitude and phase of defect have different effects on the defect field and interference intensity pattern: the defect amplitude scales only the amplitude, *i.e.*, the overall brightness, of the defect field, while the defect's phase shifts the phase of the defect field. For small-sized amplitude-only defects on blank planar substrates, when illuminated by a Gaussian beam at focus, the substrate field has a Gaussian amplitude distribution with a nearly flat phase, while the defect field has close to uniform amplitude distribution with a linear phase in an area

Optics EXPRESS

where the substrate field has significant amplitude. The linear phase is caused by the shift of the defect relative to the beam center. The substrate and defect fields are in-phase around the origin of $(f_x,f_y)$ space and the interference intensity pattern is symmetric about both $f_x$ and $f_y$, see Figs. 3(a)–3(c). Moreover, any change in defect amplitude scales the amplitude of the defect field and interference intensity pattern but does not change their patterns. Consequently, Gaussian beams at focus illuminating blank planar substrates with amplitude-only defects do not result in an asymmetry in the far-field diffraction patterns. However, when illuminated by an OAM beam at focus, the defect field is the same, but the substrate field has a donut-shaped amplitude distribution with a spiral phase distribution, as shown in Fig. 3(d). They interfere constructively around the top half of the $f_y$ axis, and destructively around the bottom half of the $f_y$ axis, resulting in significant asymmetry, as shown in Fig. 3(g). Notice that if the Gaussian and OAM beams are out of focus, the additional quadratic phase will cause a very small increase in asymmetry that is negligible compared to asymmetry from OAM beams. For simplicity, we will focus on the discussion about Gaussian and OAM beams at focus.

For small-sized phase-only defects on blank planar substrates, when illuminated by a Gaussian beam at focus, the substrate field is the same as that shown in Fig. 3(a), but the phase of the defect field is shifted by the amount of the defect phase. As a result, the substrate and defect fields are in-phase away from the origin of $(f_x,f_y)$ space, causing an asymmetry in the interference intensity pattern in the direction of the linear phase of the defect field. However, for OAM beams at focus, the interference of the donut-shaped substrate field and the phase-shifted defect field is much more complicated, especially for OAM beams with high $q$ value. In our simulation, we scanned the defect phase from 0 to $\pi$ and showed the change in the substrate and defect fields, and the interference intensity pattern in Supplementary Videos (see Visualization 1 and Visualization 2) for Gaussian and OAM beams, respectively.

### 2.3. Model-based differential CFS using two OAM beams with opposite charges

OAM beams can have either positive or negative OAM, which makes differential measurements possible. When used in conjunction with a library of reference patterns, this technique will be referred to as model-based differential OAM CFS, and the setup is shown in Fig. 1(b). At each scan point, a sample under inspection is illuminated by two OAM beams with opposite charges, one at a time. The OAM beams can be expressed as $P_{q=\pm1}(x,y) = p(x,y)e^{\pm i\varphi(x,y)}$, where $p(x,y)$ and $\varphi(x,y)$ are the amplitude and phase profiles of the OAM beams, respectively. One far-field diffraction pattern is recorded for each illumination on the detector plane, $I_{q=\pm1}(f_x,f_y)$. One diffraction pattern is subtracted from the other to form a differential measurement, for example, $M(f_x, f_y) = I_{q=+1}(f_x, f_y) - I_{q=-1}(f_x, f_y)$, which is then compared with the corresponding reference pattern, $M_r(f_x, f_y)$, to detect defects. Using the same notation, the counterparts of Eq. (2), with the first negligible term being dropped, and Eq. (3) are:

$$\begin{aligned}\Psi(f_x, f_y) &= M(f_x, f_y) - M_r(f_x, f_y)\\ &= \Im\{S(x,y)P_{q=+1}(x,y)\}\Im\{D(x,y)P_{q=+1}(x,y)\}^*\\ &- \Im\{S(x,y)P_{q=-1}(x,y)\}\Im\{D(x,y)P_{q=-1}(x,y)\}^*\\ &+ \Im\{S(x,y)P_{q=+1}(x,y)\}^*\Im\{D(x,y)P_{q=+1}(x,y)\}\\ &- \Im\{S(x,y)P_{q=-1}(x,y)\}^*\Im\{D(x,y)P_{q=-1}(x,y)\},\end{aligned} \tag{4}$$

and

$$\begin{aligned}\psi(x,y) = &\, i2cS(x+x_0, y+y_0)p(x+x_0, y+y_0)sin[\varphi(x+x_0, y+y_0)]\\ &- i2cS(-x+x_0, -y+y_0)^*p(-x+x_0, -y+y_0)sin[\varphi(-x+x_0, -y+y_0)].\end{aligned} \tag{5}$$

The sine terms in Eq. (5) originate from the subtraction of the two OAM beams with an opposite charge, *i.e.*, $e^{i\varphi(x,y)} - e^{-i\varphi(x,y)}$. It consists of the following two components: $S(x,y)p(x,y)sin\varphi(x,y)$

shifted by $(-x_0, -y_0)$ and its complex conjugate rotated by 180° and shifted by $(x_0, y_0)$, which are shown in Fig. 2(e). Similarly, since these two terms are centered at the correct defect location and its symmetric point about the origin, the correct defect location can be then determined with a two-fold ambiguity, as indicated by the two orange arrows in Fig. 2(e).

### 2.4. Model-free differential CFS using two OAM beams with opposite charges

All CFS methods discussed so far require a library of reference patterns. However, in a special case where the defect-free sample should have a reflection symmetry, the need for a library can be eliminated. This technique is referred to as model-free differential OAM CFS and its schematic is also shown in Fig. 1(b). Without loss of generality, we can define the real space coordinate such that one of these symmetric axes is on the $y$-axis, *i.e.*, $S(-x, y) = S(x, y)$. Similar to the model-based differential OAM CFS, at each scan position, the sample under inspection is illuminated twice by two OAM beams with opposite charges, and then a far-field diffraction pattern is recorded for each illumination. Importantly, one diffraction pattern, for example $I_{q=-1}(f_x, f_y)$, is first *flipped* around $f_y$-axis on the detector plane, which is the reciprocal-space counterpart of the $y$-axis. Then, the flipped diffraction pattern $I_{q=-1}(-f_x, f_y)$ is subtracted from the other diffraction pattern $I_{q=+1}(f_x, f_y)$ to get the differential measurement, $I_{q=+1}(f_x, f_y) - I_{q=-1}(-f_x, f_y)$. Using the same notation, the counterparts of Eq. (3) is:

$$\begin{aligned}\Psi(f_x, f_y) = {} & \Im\{S(x, y)P_{q=+1}(x, y)\}\Im\{D(x, y)P_{q=+1}(x, y)\}^* \\ & - \Im\{S(x, y)P_{q=+1}(x, y)\}\Im\{D(-x, y)P_{q=+1}(x, y)\}^* \\ & + \Im\{S(x, y)P_{q=+1}(x, y)\}^*\Im\{D(x, y)P_{q=+1}(x, y)\} \\ & - \Im\{S(x, y)P_{q=+1}(x, y)\}^*\Im\{D(-x, y)P_{q=+1}(x, y)\}.\end{aligned} \tag{6}$$

A model-free method is made possible because the reflection symmetry between the two OAM beams with opposite charges, $P_{q=+1}(-x, y) = P_{q=-1}(x, y)$, is the same as that of the sample, $S(-x, y) = S(x, y)$. Consequently, it is necessary that the beam center is scanned along one of the axes of the reflection symmetry of the defect-free sample. Considering one-dimensional grating samples, for example, the beam center should be scanned either perpendicular to the grating lines, or parallel to the grating lines along the center of grating lines or grooves. The former scanning scheme is easier to achieve in real experiments. To derive Eq. (6), first of all, exploiting the symmetry properties of $S(x, y)$ and $P_{q=\pm1}(x, y)$ leads to the cancellation of the first terms of $I_{q=\pm1}(f_x, f_y)$, i.e., $|\Im\{S(x, y)P_{q=-1}(x, y)\}|^2 - |\Im\{S(-x, y)P_{q=+1}(-x, y)\}|^2 = 0$. Secondly, the second term in Eq. (1) for $q = \pm1$ OAM beams, $|\Im\{D(x, y)P_{q=\pm1}(x, y)\}|^2$, is negligible because it is many orders of magnitude smaller than other terms. Furthermore, if the defect is small enough in comparison to the beam size that it can be approximated as a $\delta$-function, i.e., $D(x, y) = \delta(x - x_0, y - y_0)$, where $(x_0, y_0)$ is the position of the defect, an inverse Fourier transform of $\Psi(f_x, f_y)$ yields:

$$\begin{aligned}\psi(x, y) = {} & cS(x + x_0, y + y_0)P_{q=+1}(x + x_0, y + y_0)P_{q=+1}(x_0, y_0)^* \\ & - cS(x - x_0, y + y_0)P_{q=+1}(x - x_0, y + y_0)P_{q=+1}(-x_0, y_0)^* \\ & + c^*S(-x + x_0, -y + y_0)^*P_{q=+1}(-x + x_0, -y + y_0)^*P_{q=+1}(x_0, y_0) \\ & - c^*S(-x - x_0, -y + y_0)^*P_{q=+1}(-x - x_0, -y + y_0)^*P_{q=+1}(-x_0, y_0).\end{aligned} \tag{7}$$

Equation (7) consists of the following four terms: (1) the positive OAM beam incident onto the defect-free sample, $S(x, y)P_{q=+1}(x, y)$, shifted by $(-x_0, -y_0)$; (2) $S(x, y)P_{q=+1}(x, y)$ shifted by $(x_0, -y_0)$; (3) the complex conjugate of $S(x, y)P_{q=+1}(x, y)$, rotated by 180° and shifted by $(x_0, y_0)$; and (4) the complex conjugate of $S(x, y)P_{q=+1}(x, y)$, rotated by 180° and shifted by $(-x_0, y_0)$. Figure 2(f) shows the corresponding defect location map $\psi(x, y)$, which contains the four components introduced above. Since they are centered at $(\pm x_0, \pm y_0)$, one

Optics EXPRESS

can figure out the defect location from $\psi(x,y)$ with a four-fold ambiguity. Furthermore, as indicated by Eq. (7) and shown in Fig. 2(f), the phase of the term that centers at the defect location has the same handedness as the negative OAM beam if the differential measurement is performed with $M(f_x,f_y) = I_{q=+1}(f_x,f_y) - I_{q=-1}(-f_x,f_y)$, which decreases the ambiguity to two-fold. It is straightforward to show that if the differential measurement is performed as $M(f_x,f_y) = I_{q=-1}(f_x,f_y) - I_{q=+1}(-f_x,f_y)$, the phase of the component which centers at the defect location has the same handedness as the positive OAM beam.

## 3. Simulations and discussions

In this section, we first numerically simulate three CFS techniques on uniform samples with point defects, including (1) model-based Gaussian CFS, (2) model-based OAM CFS and (3) model-free differential OAM CFS, and compared the sensitivity of these techniques in detection of the presence of defects. Once defects are detected using the methods discussed in subsection 3.1, one can then take an inverse Fourier transform of $\Psi(f_x,f_y)$ to further locate the defects. Since the sample discussed in this section is symmetric about $x$ and $y$ axes, the model-free differential OAM CFS is be applied to perform defect detection, and the model-based differential OAM CFS is not discussed here. However, in cases where defect-free samples do not have reflection symmetry, the model-based differential OAM CFS may be used, since the model-free differential OAM CFS does not work.

### *3.1. Defect detection based on asymmetric far-field diffraction patterns*

In this section, we propose two methods to detect asymmetric far-field diffraction patterns from defects. The first method uses quadrant detectors (*QD*s), where we found that using OAM beams is advantageous over the conventional Gaussian CFS, leading to higher *QD* signal and thus higher sensitivity. The second method is based on 2D image sensors, such as cameras (*CAM*s), and is suitable for all CFS techniques, including both model-based and model-free differential OAM CFS. Although slower for data acquisition and processing speed, the camera-based method provides even higher sensitivity in defect detection. As a proof-of-concept demonstration, we limit our simulations and discussion on additive defects on a planar substrate and 1D gratings. The size of the defect is set to be $0.02w_0$, where $w_0$ is the waist radius of the Gaussian beam. In the case of inspecting a planar substrate, the illumination beam, indicated by the black dashed circle in the inset (2) of Fig. 4(a), is scanned in a 2D raster pattern across the sample under inspection. The green dashed lines denote two consecutive scan lines.

The use of *QD*s has been demonstrated to detect asymmetry in far-field diffraction patterns in Gaussian CFS, which can enhance SNR by almost two orders of magnitude [16]. To implement this method, we center far-field diffraction patterns on a detector, either by dividing a 2D image from a camera into four equal quadrants or by collecting scattered light into a quadrant photodiode. As shown in the inset (1) in Fig. 4(a), we can then calculate the horizontal asymmetry ($QD_{L-R}$) of the total number of photons between left and right quadrants, and vertical asymmetry ($QD_{T-B}$) between the top and bottom quadrants, which are defined as:

$$\begin{aligned} QD_{L-R} &= \textstyle\sum_{Q1,Q3}\Psi(f_x,f_y) - \sum_{Q2,Q4}\Psi(f_x,f_y) = \sum_{f_x<0,\ f_y}(\Psi(f_x,\ f_y) - \ \Psi(-f_x,\ f_y)), \\ QD_{T-B} &= \textstyle\sum_{Q1,Q2}\Psi(f_x,f_y) - \sum_{Q3,Q4}\Psi(f_x,f_y) = \sum_{f_x,\ f_y>0}(\Psi(f_x,\ f_y) - \ \Psi(f_x,\ -f_y)). \end{aligned} \tag{8}$$

In general, for model-based Gaussian and OAM CFS, $\Psi(f_x,f_y)$ is the difference between measured and reference patterns and is defined in Eq. (2). Specifically, for uniform planar substrates, since the reference pattern is symmetric in both $f_x$ and $f_y$ directions, $\Psi(f_x,f_y)$ can be replaced by the measured diffraction pattern.

The other approach to quantify the asymmetric diffraction patterns is the sum of the absolute value of the difference between left and right (or top and bottom) quadrants. This requires a 2D

Optics EXPRESS

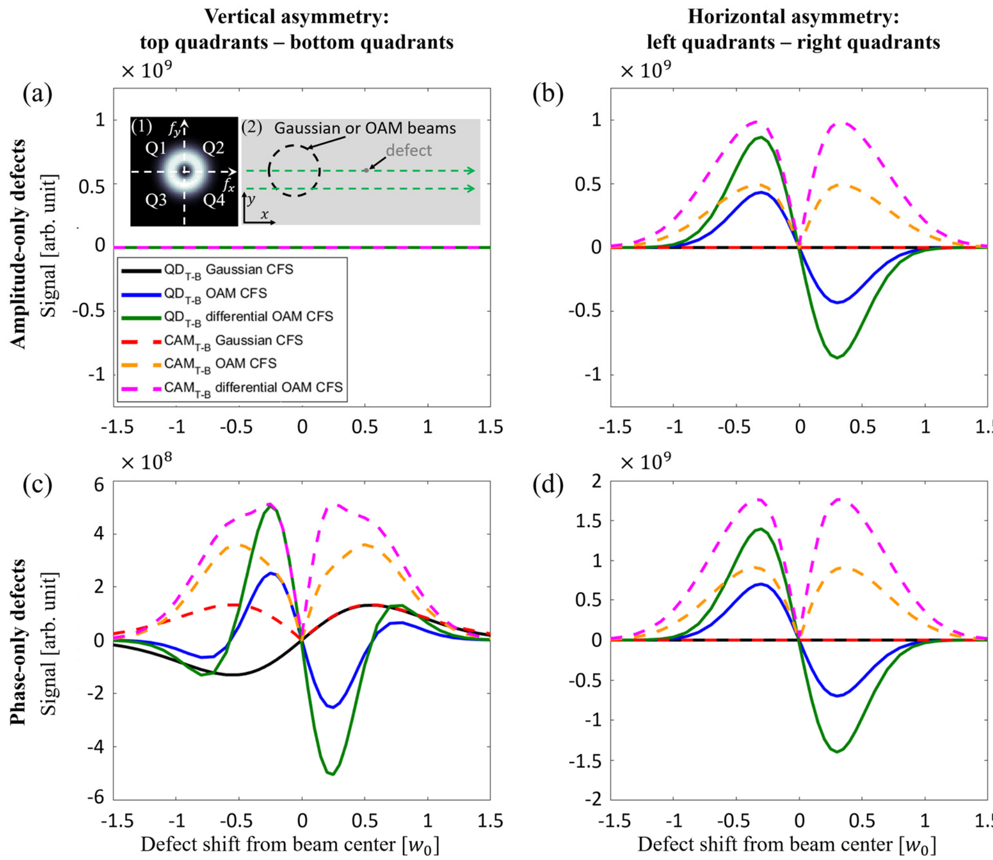


**Fig. 4. CFS signals from asymmetric far-field diffraction patterns in Gaussian CFS, OAM CFS and differential OAM CFS due to the presence of defects, detected by quadrant detectors (*QDs*) or a camera (*CAM*).** (a, b) Given an amplitude-only defect with $r = 0$, the vertical asymmetry signals ($QD_{T-B}$ and $CAM_{T-B}$) are shown in solid and dashed lines in (a), and horizontal asymmetry signals ($QD_{L-R}$ and $CAM_{L-R}$) are shown in solid and dashed lines in (b). The defect size is set to be $0.02w_0$, where $w_0$ is waist radius of the Gaussian beam, and the defect shift from beam center is normalized to $w_0$. We also varied $r$ from 0 to 1 in steps of 0.1 and made a video showing *QD* signals (see Visualization 3). (c, d) Given a phase-only defect with $\phi_0 = 135°$, the vertical and horizontal asymmetry signals are show in (c) and (d), respectively. Notice that Gaussian CFS has no sensitivity to amplitude-only defects, while OAM beams have high sensitivity. Furthermore, differential OAM CFS has twice as much signal as single OAM CFS. Lastly, *CAM* signals are higher than *QD* signals. Inset (1) of (a) shows an example far-field diffraction pattern, grouped into four equal quadrants, Q1, Q2, Q3, and Q4, of an OAM $q = +1$ beam illuminating a planar substrate with a point defect. Inset (2) shows the schematic of the scanning process for defect detection. The illumination is scanned over the sample in a 2D raster pattern, where the green dashed lines indicate two consecutive scan lines. A video with varying $\phi_0$ can be seen in Visualization 4. All subfigures share the legend shown in (a).

image sensor such as a camera and the signal can be defined as follows:

$$\begin{aligned} CAM_{L-R} &= \textstyle\sum_{f_x<0,\ f_y} |\Psi(f_x, f_y) - \Psi(-f_x, f_y)|, \\ CAM_{T-B} &= \textstyle\sum_{f_x,\ f_y<0} |\Psi(f_x, f_y) - \Psi(f_x, -f_y)|. \end{aligned} \tag{9}$$

The difference between Eq. (8) and Eq. (9) is the absolute value operation in the summand in Eq. (9). If we only consider Poisson noise, which is made possible by the state-of-the-art photon counting detector technology, the noise level of *QD* and *CAM* signals is the same given the noise in all pixels is independent and identically distributed, according to the propagation of uncertainty in statistics.

In our simulations, we investigated two types of defects, an amplitude-only defect and a phase-only defect. The substrate is set to be $S(x, y) = 0.7$ on the sample plane to model a partially reflecting flat surface. An amplitude-only defect is defined as $D(x, y) = r\,\delta(x - x_0, y - y_0)$ with $r$ being the defect amplitude and $(x_0, y_0)$ being the location of the defect on the sample plane, while a phase-only defect is defined as $D(x, y) = 0.7e^{i\phi_0}\ \delta(x - x_0, y - y_0)$ with $\phi_0$ being the relative phase between the substrate and the defect. For an amplitude-only defect with $r = 0$, the vertical and horizontal *QD* signals from diffraction pattern asymmetries as a function of scan position normalized to the Gaussian beam waist radius $w_0$ are shown in Fig. 4(a) and 4(b). We also varied $r$ from 0 to 1 in steps of 0.1 and made a video showing *QD* signals (see Visualization 3). Gaussian beams at focus have no sensitivity at all to amplitude-only defects because the diffraction patterns are perfectly symmetric, while OAM beams at focus are very sensitive due to the spiral phase structure. For a phase-only defect with $\phi_0 = 135°$, the vertical and horizontal *QD* signals are shown in Fig. 4(c) and 4(d) and a video with varying $\phi_0$ between 0 and 1 in steps of 5 degrees can be seen in Visualization 4. Even though Gaussian beams are sensitive to phase-only defects, OAM beams generally have 2-10 times higher signal levels, a significant improvement. An obvious advantage of using quadrant photodiodes is the high-speed data acquisition and processing and thus high inspection throughput, at any wavelength from visible light to EUV.

The *QD*-based method only captures the difference in the total number of photons between different quadrants, instead of the photon distribution or diffraction patterns within each quadrant. As a result, the detailed, pixel-by-pixel information about the asymmetry is lost. To overcome this, we now investigate the camera-based method. The vertical and horizontal *CAM* signals of amplitude-only and phase-only defects are shown in Fig. 4(a)–4(d). It is evident that the camera-based method can further improve the signal level, compared to the *QD*-based method, and provides even higher sensitivity in defect detection. However, for higher sensitivity, data acquisition and processing time will be longer. The speed limit could be relaxed and eventually overcome given the high-speed CMOS cameras readily available for visible light and just released commercially for EUV and soft x-ray wavelengths.

### *3.2. Effect of varying OAM charges on sensitivity*

We also studied the effect of varying OAM charge $q$ on *QD* and *CAM* signals in model-based Gaussian and OAM CFS. As shown in Figs. 5(b), 5(e), 5(f), when the OAM charge varies from $q = 0$ (Gaussian beams) to $q = +5$, the *QD* signals for both amplitude- and phase-only defects first increase and then decrease. We attribute this phenomenon to the fact that an OAM beam with larger $q$ diverges faster and the interference between the sample and defect fields may change accordingly. On the other hand, the *CAM* signals increase monotonically by a factor of at least 5 as the OAM charge increases from 0 to 5 as shown in Figs. 5(d), 5(g), 5(h). Higher signal gain is expected if higher OAM charge beams are used. This also indicates that OAM beams with larger charges result in more asymmetry in photon distribution, but not necessarily in the total number of photons of each quadrant.

### *3.3. Generalization of OAM beam-based CFS to 1D gratings*

Our simulations so far are limited to uniform planar substrates with additive point defects. The types of samples that work under this framework are defined by the assumption made in Sections 2.3 and 2.4: the defect-free sample is symmetric about some axis. It follows that these techniques can be easily generalized to inspect more complex samples with reflection symmetry

Optics EXPRESS

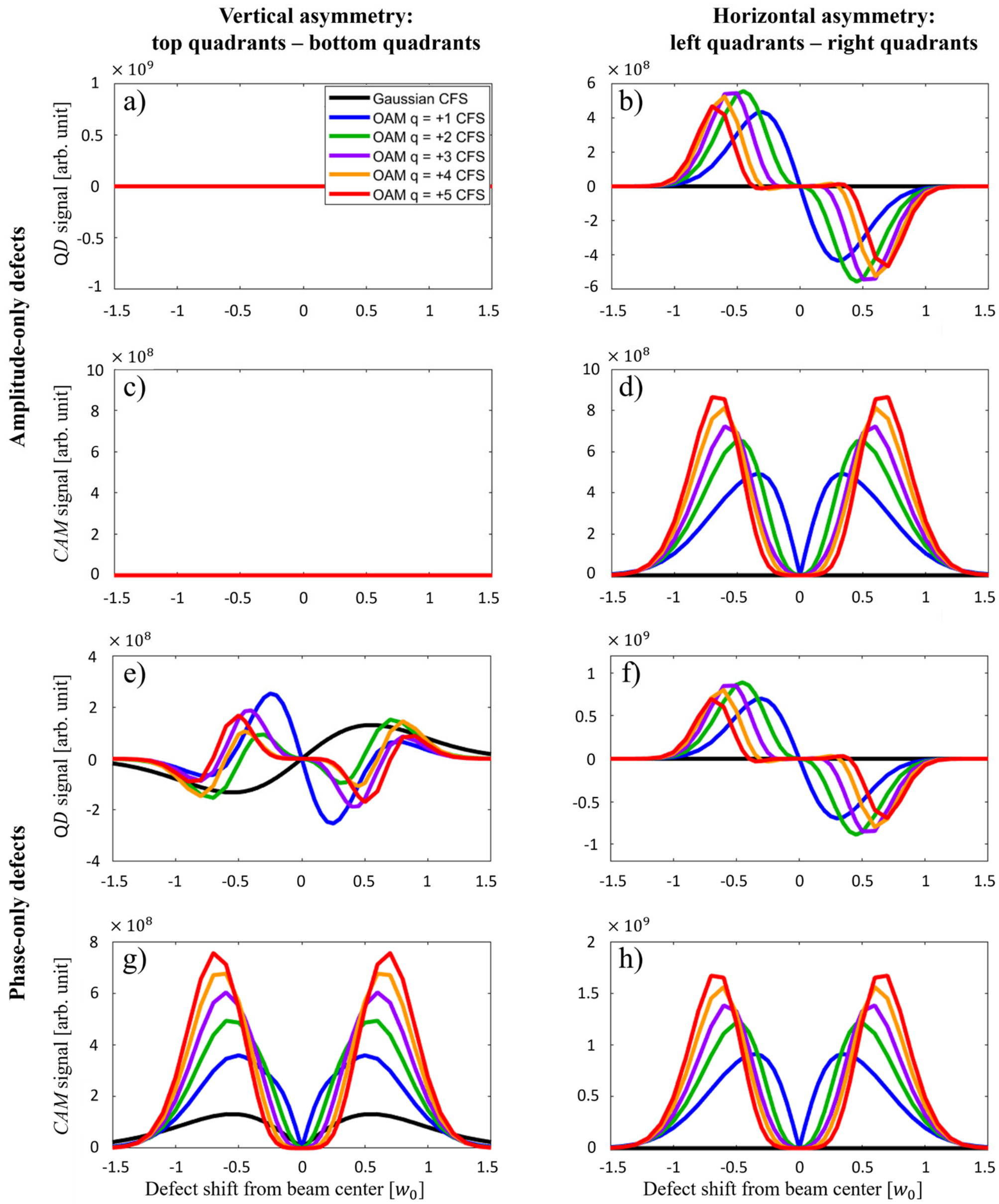


**Fig. 5. Effect of varying OAM charges in both model-based Gaussian CFS and OAM CFS.** Given an amplitude-only defect, (a, b) show the vertical and horizontal *QD* asymmetry signals ($QD_{T-B}$ and $QD_{L-R}$) and (c, d) show the vertical and horizontal *CAM* asymmetry signals ($CAM_{T-B}$ and $CAM_{L-R}$) for Gaussian and OAM beams with different charges. Given a phase-only defect, (e, f) show vertical and horizontal *QD* asymmetry signals and (g, h) show the vertical and horizontal *CAM* signals for Gaussian and OAM beams. All subfigures share the legend shown in (a). Note that the monotonic signal increases only occur in the camera-based method, while the signals will get maximized at particular OAM charges in the *QD*-based method.

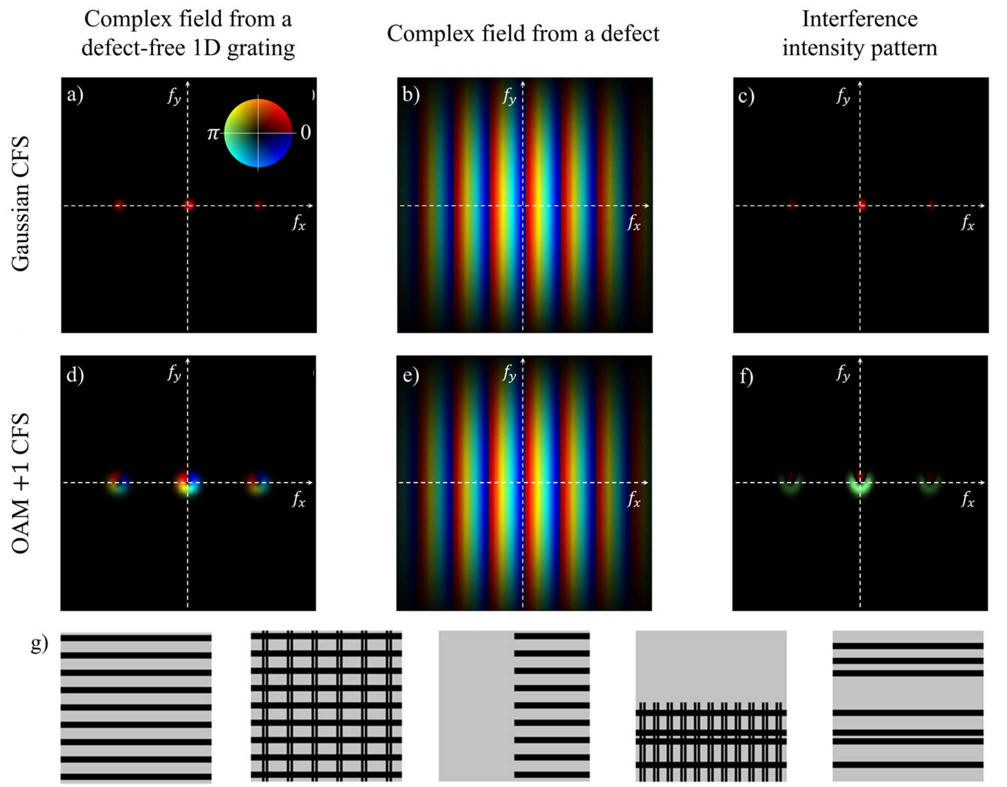


**Fig. 6. The characteristics of far-field diffraction patterns resulting from Gaussian and OAM beam illumination of 1D line grating structures including amplitude-only defects.** (a) and (b) show the complex field from the defect-free 1D grating and that from the defect, *i.e.*, $\mathfrak{I}\{S(x,y)P_q(x,y)\}$ and $\mathfrak{I}\{D(x,y)P_q(x,y)\}$ in Eq. (1), in the far-field from Gaussian CFS. The defect is assumed to be located to the right of the beam for the discussion. (c) shows the interference intensity pattern, i.e., $\mathfrak{I}\{S(x,y)P_{q=0}(x,y)\}\mathfrak{I}\{D(x,y)P_{q=0}(x,y)\}^* + \mathfrak{I}\{S(x,y)P_{q=0}(x,y)\}^*\mathfrak{I}\{D(x,y)P_{q=0}(x,y)\}$. Similar plots for OAM ±1 CFS are shown in (d-f). The interference intensity pattern of OAM CFS in (f) shows significant asymmetry due to the spiral phase of the OAM beam. The color wheel for complex field representation is shown in the top right corner of (a), where amplitude and phase are represented by brightness and hue, respectively. (g) shows several example samples that can be inspected using any of the OAM CFS techniques presented here, including periodic 1D and 2D gratings, ends of these gratings and aperiodic set of lines. These example samples have reflection symmetry in at least one direction.

[see Fig. 6(g)], such as 1D and 2D gratings and aperiodic sets of lines that are widely used in photolithography in semiconductor manufacturing. To support this statement, we briefly investigate point defects on a 1D granting. We follow a similar analysis from Gaussian and OAM CFS on uniform planar substrates discussed before in subsection 2.2.

Figure 6(a) shows the complex field from a defect-free 1D grating, and Fig. 6(b) shows a complex field from an amplitude-only defect, and Fig. 6(c) is the resulting interference intensity pattern. The defect size is $0.02w_0$, and it is located $0.43w_0$ away from the beam center, which is also where the OAM beam with $q = 1$ reaches maximum intensity. The horizontal linear phase in Fig. 6(b) is caused by the shift of the defect to the right in real space relative to the center of the illumination beam. Similarly, Fig. 6(d-f) shows these three plots from an OAM beam with $q = 1$ illuminating on the same sample. Clearly, the interference intensity pattern from a Gaussian beam shows little asymmetry in all three diffraction orders, while that from an OAM beam exhibits significant asymmetry in all diffraction orders. The results in Fig. 6 are presented the same way as those in Fig. 3. As in the case of planer substrates (Fig. 3), in this case with 1D gratings (Fig. 6), constructive interference between the substrate and defect fields occurs in the top half of the field where they are in phase, while destructive interference happens in the bottom half of the field where they are out of phase. As a result, we can exploit the same *QD* or *CAM* methods to detect the asymmetric patterns and identify the presence and the locations of these defects on 1D line gratings. Analysis of 2D grating samples can be accomplished in a similar manner.

### 3.4. Discussions and outlook

We now consider how noise affects our proposed CFS techniques. Common noise sources include shot noise, detector noises, sample noises (e.g., surface roughness), etc. One major challenge in defect detection on blank wafers is to distinguish between defect signals and the noise generated by pattern roughness, especially for dark-field CFS techniques. The dark-field CFS techniques block the specular reflection and capture the high-angle scattered light that in principle exists only in the presence of defects. However, the presence of noises such as those from surface roughness will also contribute to high-angle scattering, making it challenging to distinguish real defects from noises. As for our proposed OAM-based CFS techniques, they are bright-field based and detect defects by measuring asymmetries in the far-field diffraction patterns. Because the above noise sources are mostly isotropic in the micrometer-size scale, they introduce limited asymmetries in the far-field diffraction patterns, thus making the proposed OAM-based bright-field CFS techniques more robust.

In our simulation, we limited our focus to OAM CFS of uniform planar substrates and 1D gratings with additive point defects. However, we believe that this technique can be generalized easily to inspect more complex samples. Future efforts should be devoted to modeling light-matter interaction using more general theories, such as finite element methods or rigorous coupled-wave analysis [31,32], which can take complex 3D nanostructures or multiple scattering events into account if needed for some sample types. Further evaluations on the impact of defects on printed patterns such as the actinic aerial image seen by photolithographic scanners are also needed, because the volumetric effects could lead to the "self-healing" of certain defects, reducing their printability. Furthermore, we anticipate the use of machine learning to help rapidly identify OAM CFS diffraction patterns from different samples under inspection, as they are shown to be efficient and powerful tools for defect detection and classification [33]. We also envision the adaption of OAM beams or other phase or wavefront structured beams for general purpose scatterometry measurements beyond defect inspection such as grazing-incidence, small-angle, or wide-angle x-ray scattering.

## 4. Conclusion

In this work, we presented a set of novel optical scatterometry techniques for high-sensitivity in-line defect inspection by OAM-beam-based bright-field CFS. Our numerical experiments demonstrated the feasibility of such techniques by studying amplitude and phase point defects on planar substrates and 1D gratings. Our proof-of-concept demonstrations show that OAM CFS outperforms conventional model-based Gaussian CFS by up to an order of magnitude. Moreover, differential OAM CFS techniques using opposite charges make the model-free CFS possible, eliminating the need for a reference library in cases where the defect-free sample has reflection symmetry. In terms of the two data acquisition and processing methods we proposed, the quadrant detector-based method works faster and is less computationally expensive, while the camera-based method has the potential to provide higher sensitivity. The concept of our new techniques is general, and thus we expect that these techniques can be implemented as next-generation visible, ultraviolet, EUV, x-ray inspection tools. This could address demanding industrial metrologies such as mask, reticle, and wafer inspection, as the semiconductor industry marches toward sub-10 nm photolithography-based manufacturing.

**Funding.** STROBE: A National Science Foundation Science & Technology Center (DMR 1548924); Defense Advanced Research Projects Agency (W31P4Q-17-C-0104); Defense Advanced Research Projects Agency (140D0419C0094); China Scholarship Council (201806260040).

**Disclosures.** H.K.: KMLabs Inc. (I, E, P). M.M.: KMLabs Inc. (I, P). Other authors declare no conflicts of interest.

## References

1. C. J. Raymond, M. R. Murnane, S. Sohail, H. Naqvi, and J. R. McNeil, "Metrology of subwavelength photoresist gratings using optical scatterometry," J. Vac. Sci. Technol., B: Microelectron. Process. Phenom. **13**(4), 1484–1495 (1995).
2. C. J. Raymond, "Overview of scatterometry applications in high volume silicon manufacturing," AIP Conf. Proc. **788**, 394–402 (2005).
3. M. H. Madsen and P. Hansen, "Scatterometry – fast and robust measurements of nano-textured surfaces," Surf. Topogr.: Metrol. Prop. **4**(2), 023003 (2016).
4. H. J. Levinson, *Principles of Lithography*, 2nd ed. (SPIE, 2005).
5. C. Wagner and N. Harned, "EUV lithography: Lithography gets extreme," Nat. Photonics **4**(1), 24–26 (2010).
6. E. Agocs, B. Bodermann, S. Burger, G. Dai, J. Endres, P.-E. Hansen, L. Nielson, M. H. Madsen, S. Heidenreich, M. Krumrey, B. Loechel, J. Probst, F. Scholze, V. Soltwisch, and M. Wurm, "Scatterometry reference standards to improve tool matching and traceability in lithographical nanomanufacturing," Proc. SPIE **9556**, 955610 (2015).
7. A. Rundquist, C. G. Durfee III, Z. Chang, C. Herne, S. Backus, M. M. Murnane, and H. C. Kapteyn, "Phase-Matched Generation of Coherent Soft X-rays," Science **280**(5368), 1412–1415 (1998).
8. R. A. Bartels, A. Paul, H. Green, H. C. Kapteyn, M. M. Murnane, S. Backus, I. P. Christov, Y. Liu, D. Attwood, and C. Jacobsen, "Generation of Spatially Coherent Light at Extreme Ultraviolet Wavelengths," Science **297**(5580), 376–378 (2002).
9. D. E. Couch, D. D. Hickstein, D. G. Winters, S. J. Bucks, M. S. Kirchner, S. R. Domingue, J. J. Ramirez, C. G. Durfee, M. M. Murnane, and H. Kapteyn, "Ultrafast 1 MHz vacuum-ultraviolet source via highly cascaded harmonic generation in negative-curvature hollow-core fibers," Optica **7**(7), 832–837 (2020).
10. M. D. Seaberg, B. Zhang, D. F. Gardner, E. R. Shanblatt, M. M. Murnane, H. C. Kapteyn, and D. E. Adams, "Tabletop nanometer extreme ultraviolet imaging in an extended reflection mode using coherent Fresnel ptychography," Optica **1**(1), 39–44 (2014).
11. D. F. Gardner, M. Tanksalvala, E. R. Shanblatt, X. Zhang, B. R. Galloway, C. L. Porter, R. Karl Jr, C. Bevis, D. E. Adams, H. C. Kapteyn, M. M. Murnane, and G. F. Mancini, "Subwavelength coherent imaging of periodic samples using a 13.5 nm tabletop high-harmonic light source," Nat. Photonics **11**(4), 259–263 (2017).
12. R. M. Karl Jr., G. F. Mancini, J. L. Knobloch, T. D. Frazer, J. N. Hernandez-Charpak, B. Abad, D. F. Gardner, E. R. Shanblatt, M. Tanksalvala, C. L. Porter, C. S. Bevis, D. E. Adams, H. C. Kapteyn, and M. M. Murnane, "Full-field imaging of thermal and acoustic dynamics in an individual nanostructure using tabletop high harmonic beams," Sci. Adv. **4**(10), eaau4295 (2018).
13. C. Chen, Z.-S. Tao, A. Carr, P. Matyba, T. Szilvási, S. Emmerich, M. Piecuch, M. Keller, D. Zusin, S. Eich, M. Rollinger, W.-J. You, S. Mathias, U. Thumm, M. Mavrikakis, M. Aeschlimann, P. M. Oppeneer, H. Kapteyn, and M. Murnane, "Distinguishing attosecond electron-electron scattering and screening in transition metals," Proc. Natl. Acad. Sci. U.S.A. 114(27), E5300–E5307 (2017).
14. P. Tengdin, C. Gentry, A. Blonsky, D. Zusin, M. Gerrity, L. Hellbrück, M. Hofherr, J. Shaw, Y. Kvashnin, E. K. Delczeg-Czirjak, M. Arora, H. Nembach, T. J. Silver, S. Mathias, M. Aeschlimann, H. Kapteyn, D. Thonig, K. Koumpouras, O. Eriksson, and M. M. Murnane, "Direct light-induced spin transfer between different elements in a spintronic Heusler material via femtosecond laser excitation," Sci. Adv. **6**(3), eaaz1100 (2020).
15. M. Tanksalvala, C. L. Porter, Y. Esashi, B. Wang, N. W. Jenkins, Z. Zhang, G. P. Miley, J. L. Knobloch, B. McBennett, N. Horiguchi, S. Yazdi, J. Zhou, M. N. Jacobs, C. S. Bevis, R. M. Karl Jr., P. Johnsen, D. Ren, L. Waller, D. E. Adams, S. L. Cousin, C.-T. Liao, J. Miao, M. Gerrity, H. C. Kapteyn, and M. M. Murnane, "Non-Destructive, High-Resolution, Chemically Specific, 3D Nanostructure Characterization using Phase-Sensitive EUV Imaging Reflectometry," Sci. Adv. in press.
16. O. E. Gawhary and S. J. H. Petra, "Method and apparatus for determining structure parameters of microstructures," US Patent application 9,175,951B2 (11 March 2015).
17. S. Roy, A. C. Assafro, S. F. Pereira, and H. P. Urbach, "Coherent Fourier scatterometry for detection of nanometer-sized particles on a planar substrate surface," Opt. Express **22**(11), 13250–13262 (2014).
18. S. Lozenko, T. Shapoval, G. Ben-Dov, Z. Lindenfeld, B. Schulz, L. Fuerst, C. Harting, R. Haupt, M. Ruhm, and R. Wang, "Matching between simulations and measurements as a key driver for reliable overlay target design," *Metrology,*

Optics EXPRESS

*Inspection, and Process Control for Microlithography XXXII*, vol 10585 V. A. Ukraintsev, ed., International Society for Optics and Photonics (SPIE, 2018), pp. 314–325.

19. L. Allen, M. W. Beijersbergen, R. J. C. Spreeuw, and J. P. Woerdman, "Orbital angular momentum of light and the transformation of Laguerre-Gaussian laser modes," Phys. Rev. A **45**(11), 8185–8189 (1992).
20. A. E. Willner, H. Huang, Y. Yan, Y. Ren, N. Ahmed, G. Xie, C. Bao, L. Li, Y. Cao, Z. Zhao, J. Wang, M. P. J. Lavery, M. Tur, S. Ramachandran, A. F. Molisch, N. Ashrafi, and S. Ashrafi, "Optical communication using orbital angular momentum beams," Adv. Opt. Photonics **7**(1), 66–106 (2015).
21. J. P. Torres and L. Torner, *Twisted photons: applications of light with orbital angular momentum*, (John Wiley, 2011).
22. L. Torner and J. P. Torres, "Digital spiral imaging," Opt. Express **13**(3), 873–881 (2005).
23. M. Zürch, C. Kern, P. Hansinger, A. Dreischuh, and C. Spielmann, "Strong-field physics with singular light beams," Nat. Phys. **8**(10), 743–746 (2012).
24. L. Rego, K. M. Dorney, N. J. Brooks, Q. L. Nguyen, C.-T. Liao, J. S. Román, D. E. Couch, A. Liu, E. Pisanty, M. Lewenstein, L. Plaja, H. C. Kapteyn, M. M. Murnane, and C. Hernández-García, "Generation of extreme-ultraviolet beams with time-varying orbital angular momentum," Science **364**(6447), eaaw9486 (2019).
25. K. M. Dorney, L. Rego, N. J. Brooks, J. S. Román, C.-T. Liao, J. L. Ellis, D. Zusin, C. Gentry, Q. L. Nguyen, J. M. Shaw, A. Picón, L. Plaja, H. C. Kapteyn, M. M. Murnane, and C. Hernández-García, "Controlling the polarization and vortex charge of attosecond high-harmonic beams via simultaneous spin-orbit momentum conservation," Nat. Photonics **13**(2), 123–130 (2019).
26. M. Harris, C. A. Hill, and J. M. Vaughan, "Optical helices and spiral interference fringes," Opt. Commun. **106**(4-6), 161–166 (1994).
27. J. M. Hickmann, E. J. S. Fonseca, W. C. Soares, and S. Chávez-Cerda, "Unveiling a truncated optical lattice associated with a triangular aperture using light's orbital angular momentum," Phys. Rev. Lett. **105**(5), 053904 (2010).
28. Y. Esashi, C.-T. Liao, B. Wang, N. Brooks, K. M. Dorney, C. Hernández-García, H. Kapteyn, and M. Murnane, "Ptychographic amplitude and phase reconstruction of bichromatic vortex beams," Opt. Express **26**(26), 34007–34015 (2018).
29. S. Peterhansel, M. L. Godecke, V. F. Paz, K. Frenner, and W. Osten, "Detection of overlay error in double patterning gratings using phase-structured illumination," Opt. Express **23**(19), 24246–24256 (2015).
30. S. Peterhansel, M. L. Godecke, K. Frenner, and W. Osten, "Phase-structured illumination as a tool to detect nanometer asymmetry," J. Micro/Nanolith. MEMS MOEMS **15**(4), 044005 (2016).
31. M. G. Moharam and T. K. Gaylord, "Rigorous coupled-wave analysis of planar-grating diffraction," J. Opt. Soc. Am. **71**(7), 811–818 (1981).
32. X. Wei, A. J. H. Wachters, and H. P. Urbach, "Finite-element model for three-dimensional optical scattering problems," J. Opt. Soc. Am. A **24**(3), 866–881 (2007).
33. D. Kolenvo and S. F. Pereira, "Machine learning techniques applied for the detection of nanoparticles on surfaces using coherent Fourier scatterometry," Opt. Express **28**(13), 19163–19186 (2020).